Received: 9 May 2019 | Revised: 16 December 2019 | Accepted: 26 January 2020

DOI: 10.1002/fld.4818

RESEARCH ARTICLE

WILEY

An adaptive moving finite element method for steady low Mach number compressible combustion problems

Zhen Sun[1] | **Malte Braack**[2] | **Jens Lang**[1]

[1]Technical University of Darmstadt, Dolivostraße 15, 64293 Darmstadt, Germany

[2]Christian-Albrechts-Universität zu Kiel, Westring 383, 24098 Kiel, Germany

Correspondence
Jens Lang, Technical University of Darmstadt, Dolivostraße 15, 64293 Darmstadt, Germany.
Email: lang@mathematik.tu-darmstadt.de

Funding information
Deutsche Forschungsgemeinschaft, DFG GSC1070

Summary

This work surveys an *r*-adaptive moving mesh finite element method for the numerical solution of premixed laminar flame problems. Since the model of chemically reacting flow involves many different modes with diverse length scales, the computation of such a problem is often extremely time-consuming. Importantly, to capture the significant characteristics of the flame structure when using detailed chemistry, a much more stringent requirement on the spatial resolution of the interior layers of some intermediate species is necessary. Here, we propose a moving mesh method in which the mesh is obtained from the solution of so-called moving mesh partial differential equations. Such equations result from the variational formulation of a minimization problem for a given target functional that characterizes the inherent difficulty in the numerical approximation of the underlying physical equations. Adaptive mesh movement has emerged as an area of intense research in mesh adaptation in the last decade. With this approach, points are only allowed to be shifted in space leaving the topology of the grid unchanged. In contrast to methods with local refinement, data structure hence is unchanged and load balancing is not an issue as grid points remain on the processor where they are. We will demonstrate the high potential of moving mesh methods for effectively optimizing the distribution of grid points to reach the required resolution for chemically reacting flows with extremely thin boundary layers.

KEYWORDS

adaptive moving meshes, low Mach number combustion, Rosenbrock time integrators, stabilized finite elements

1 | INTRODUCTION

The numerical simulation of chemically reacting flows with detailed chemistry is still a challenging task due to the presence of a large range of multi-scale aspects. High spatial resolution is needed in the vicinity of the flame zone, while simultaneously coarser meshes can be used in regions with relatively large flow structures, for example, downstream of the flame. Adaptive mesh refinement (AMR) based on dynamically refining or coarsening the computational

mesh to match local features has proven to be a very efficient strategy to perform a multi-scale combustion simulation. An overview of the basic design concepts used to develop block-structured AMR algorithms for the low Mach number model has been given by Bell and Day.[1] Two of the authors, Braack and Lang, have also been contributing to the development of AMR methods.[2-5] However, since reacting flow applications with detailed chemistry and transport models already tend to be significantly complex, an AMR implementation on parallel computers might quickly become prohibitively intricate. In such a situation, adaptive moving mesh (AMM) methods are considered to be an attractive alternative since the mesh topology and hence the underlying data structures are left unchanged. Such methods have become available through the implementation of variational principles that define a moving mesh as the solution of so-called moving mesh partial differential equations (MMPDEs) introduced by Huang and Russell, see Reference 6 for a thorough overview. Recently, AMMs have been successfully applied to large eddy simulations of complex turbulent flows by Liersch et al.[7]

In this article, we investigate the application of the AMM technique to steady low Mach number compressible combustion problems in two spatial dimensions. Special emphasize is put on the design of the monitor function that constitutes the heart of the MMPDE and links the movement of the grid points to the physical solution. We will discuss two approaches that are based on the gradient and the curvature of selected chemical components, respectively. The latter one is motivated by a standard error estimate of the interpolation error. The steady combustion model is discretized by stabilized linear finite elements that use pressure stabilization and streamline diffusion to enhance the main diagonal of the resulting algebraic system. A pseudo linearly implicit time-stepping scheme is applied to solve the highly nonlinear algebraic systems. Two examples are considered to demonstrate the potential of our AMM method: a benchmark three-component ozone decomposition and a methane flame in the practical application of a prototype lamelle burner from the Bosch company.

2 | THEORETICAL FUNDAMENTALS OF REACTIVE FLOWS

2.1 | Models for stationary chemically reacting flows

We denote the flow velocities by $\boldsymbol{v}$, the pressure by p, the temperature by T, and the density by ρ. Furthermore, $\boldsymbol{w} = (w_1, \dots, w_{n_s})^T$ is defined as the vector of mass fractions w_i of the i-th species, where $i = 1, \dots, n_s$. The basic equations for a stationary reactive viscous flow express the conservation and balance laws for the total mass, momentum, energy, and each species, respectively, accomplished by the equation of state:

$$\nabla \cdot (\rho \boldsymbol{v}) = 0, \tag{1}$$

$$\rho(\boldsymbol{v} \cdot \nabla)\boldsymbol{v} + \nabla p + \nabla \cdot \boldsymbol{\tau} = \rho \boldsymbol{g}, \tag{2}$$

$$\rho \boldsymbol{v} \cdot \nabla w_i + \nabla \cdot (\rho D_i \nabla w_i) = M_i \, \dot{w}_i(T, \boldsymbol{\omega}), \quad i = 1, \dots, n_s, \tag{3}$$

$$c_p \rho \boldsymbol{v} \cdot \nabla T - \nabla \cdot (\lambda \nabla T) - \boldsymbol{v} \cdot \nabla p + \boldsymbol{\tau} : \nabla \boldsymbol{v} = -\sum_{i=1}^{n_s} h_i M_i \dot{w}_i(T, \boldsymbol{w}), \tag{4}$$

$$p = \frac{\rho R T}{\overline{M}}, \quad \overline{M} = \left(\sum_{i=1}^{n_s} \frac{w_i}{M_i} \right)^{-1}, \tag{5}$$

where $\boldsymbol{g}$ is the gravitational force and c_p is the heat capacity of the mixture at constant pressure. For each species, M_i is the molecular weight, h_i its (mass-)specific enthalpy, $\dot{w}_i$ its molar production rate, and D_i its mass diffusion coefficient. The viscous stress tensor $\boldsymbol{\tau}$ is given by

$$\boldsymbol{\tau} = -\mu \left(\nabla \boldsymbol{v} + (\nabla \boldsymbol{v})^T - \frac{2}{3} (\nabla \cdot \boldsymbol{v}) \mathbf{I} \right), \tag{6}$$

with μ being the dynamic viscosity of the fluid. Compressible flow equations admit material and acoustic waves that propagate at velocity $\boldsymbol{v}$ and speed of sound c, respectively. In most practical combustion systems, the flow is in the low Mach number regime, that is, $M = |\boldsymbol{v}|/c \ll 1$. This disparity in scales can be exploited to compute combustion problems

much more efficiently. A rigorous low Mach number asymptotic analysis[8] for the behavior $M \to 0$ shows that the total pressure can be decomposed as

$$p(\boldsymbol{x}) = P_{\text{th}} + p_{\text{hyd}}(\boldsymbol{x}), \tag{7}$$

where P_{th} is the constant thermodynamic pressure and $p_{\text{hyd}}(\boldsymbol{x})$ is the hydrodynamic pressure. With this decomposition, P_{th} defines the thermodynamic state and p_{hyd} plays the role of a Lagrange multiplier to constrain the flow so that the thermodynamic pressure is equilibrated everywhere in space. Hence, compressibility effects due to chemical heat release and other thermal processes are retained while acoustic wave propagation is entirely eliminated. Eventually, the simplified low Mach number approximation for steady compressible reactive flows becomes[9]

$$\nabla \cdot \boldsymbol{v} = \frac{1}{T}\boldsymbol{v} \cdot \nabla T - \frac{1}{\overline{M}}\boldsymbol{v} \cdot \nabla \overline{M}, \tag{8}$$

$$\rho(\boldsymbol{v} \cdot \nabla)\boldsymbol{v} + \nabla p_{\text{hyd}} - \nabla \cdot (\mu \nabla \boldsymbol{v}) = \rho \boldsymbol{g}, \tag{9}$$

$$\rho \boldsymbol{v} \cdot \nabla w_i + \nabla \cdot (\rho D_i \nabla w_i) = M_i \, \dot{w}_i(T, \boldsymbol{w}), \quad i = 1, \dots, n_s, \tag{10}$$

$$c_p \rho \boldsymbol{v} \cdot \nabla T - \nabla \cdot (\lambda \nabla T) = -\sum_{i=1}^{n_s} h_i M_i \dot{w}_i(T, \boldsymbol{w}), \tag{11}$$

$$\rho = \frac{P_{\text{th}} \overline{M}}{RT}, \quad \overline{M} = \left(\sum_{i=1}^{n_s} \frac{w_i}{M_i} \right)^{-1}. \tag{12}$$

Here, we have differentiated the new equation of state in (12) to derive a constraint on the velocity in (8). As usual, parts of the stress tensor have been absorbed into p_{hyd}. We will only consider $n_s - 1$ species equations together with the requirement $\sum_{i=1}^{n_s} w_i = 1$ to keep mass conservation and the computation of diffusion velocities consistent.[10] Since only laminar flames are considered, the influence of the gravitation in (9) is also often neglected. We set $P_{\text{th}} = 101\,325$ Pa in our applications.

2.2 | Finite element discretization

To simplify the notation and write the system (8)-(12) in a more compact form, we extend the vector of mass fractions by $w_0 := T$ and introduce

$$\nu_0 = \lambda, \quad \nu_i = \rho D_i, \quad i = 1, \dots, n_s, \tag{13}$$

for the diffusion coefficients of all components of $\boldsymbol{w} = (w_0, \dots, w_{n_s})^T$. With the new quantities

$$\boldsymbol{\beta} = \rho \boldsymbol{v}, \quad \boldsymbol{m} = \overline{M}^{-1} \nabla \overline{M}, \quad l = (\rho T)^{-1}, \tag{14}$$

$$f_0(\boldsymbol{w}) = -\sum_{i=1}^{n_s} h_i M_i \dot{w}_i, \quad f_i(\boldsymbol{w}) = M_i \, \dot{w}_i, \; i = 1, \dots, n_s, \tag{15}$$

and the convention that $\overline{\boldsymbol{\beta}} = c_p \boldsymbol{\beta}$ for the temperature equation ($i = 0$) and $\overline{\boldsymbol{\beta}} = \boldsymbol{\beta}$ otherwise, the stationary low Mach number system can be rewritten in the condensed form

$$\nabla \cdot \boldsymbol{v} - l \boldsymbol{\beta} \cdot \nabla w_0 + \boldsymbol{v} \cdot \boldsymbol{m} = 0, \tag{16}$$

$$(\boldsymbol{\beta} \cdot \nabla)\boldsymbol{v} - \nabla \cdot (\mu \nabla \boldsymbol{v}) + \nabla p_{\text{hyd}} = \rho \boldsymbol{g}, \tag{17}$$

$$\overline{\boldsymbol{\beta}} \cdot \nabla w_i - \nabla \cdot (\nu_i \nabla w_i) = f_i(\boldsymbol{w}), \; i = 0, \dots, n_s. \tag{18}$$

For the presentation of the finite element approximation of this system, we follow the approach presented in References [9, section 2] and 11.

Let $\Omega \in \mathbb{R}^2$ be our bounded computational domain with polygonal boundary $\partial\Omega$. Introducing the inner product and norm

$$(f,g) := \int_\Omega f(\boldsymbol{x})g(\boldsymbol{x})\, d\boldsymbol{x}, \quad \|f\| := \left(\int_\Omega |f(\boldsymbol{x})|^2\, d\boldsymbol{x}\right)^{1/2}, \tag{19}$$

the Lebesgue space of all square-integrable functions on Ω, $L^2(\Omega)$, is defined by all functions $f(\boldsymbol{x})$ with $\|f\| < \infty$. The functions from $L^2(\Omega)$ with square-integrable generalized first-order derivatives form the Sobolev space $H^1(\Omega)$. We will use certain subspaces of these two spaces to set up a variational weak formulation for (16)-(18), namely

$$p \in Q = L^2(\Omega)/\mathbb{R}, \qquad \boldsymbol{v} \in H \subset \left(H^1(\Omega)\right)^2, \qquad \boldsymbol{w} \in R \subset \left(H^1(\Omega)\right)^{n_s+1}. \tag{20}$$

Note that the pressure is determined only modulo constants, which is expressed by the special construction of the space Q. The solution triple $\boldsymbol{u} := (p, \boldsymbol{v}, \boldsymbol{w})$ is now an element of the space $V := Q \times H \times R$. Testing the equations (16)-(18) with a function $\boldsymbol{\phi} = (\theta, \chi, \boldsymbol{\pi}) \in V$, integrating over Ω, and applying integration by parts for the diffusive terms and the pressure gradient yields the variational nonlinear equations

$$\boldsymbol{u} \in V: \quad A(\boldsymbol{u}, \boldsymbol{\phi}) = 0 \quad \text{for all } \boldsymbol{\phi} \in V, \tag{21}$$

with the semi-linear form

$$\begin{aligned} A(\boldsymbol{u}, \boldsymbol{\phi}) := {} & (\nabla \cdot \boldsymbol{v}, \theta) - (l\boldsymbol{\beta} \cdot \nabla w_0, \theta) + (\boldsymbol{v} \cdot \boldsymbol{m}, \theta) \\ & + ((\boldsymbol{\beta} \cdot \nabla)\boldsymbol{v}, \chi) + (\mu \nabla \boldsymbol{v}, \nabla \chi) - (p_{\text{hyd}}, \nabla \cdot \chi) - (\rho \boldsymbol{g}, \chi) \\ & + \sum_{i=0}^{n_s} \{(\overline{\boldsymbol{\beta}} \cdot \nabla w_i, \pi_i) + (\nu_i \nabla w_i, \nabla \pi_i) - (f_i(\boldsymbol{w}), \pi_i)\}. \end{aligned} \tag{22}$$

Here, for simplicity, we have used the free-stream outflow condition and homogeneous Dirichlet conditions. Other boundary conditions can be handled by natural modifications.

We will now describe our finite element approximation. First, we decompose $\overline{\Omega}$ into a regular partition of triangles $\mathcal{T}_h = \{K\}$ and define the conforming finite element space of continuous piecewise linear functions by

$$S_h := \{f \in C^0(\overline{\Omega}) : f_{|K} \in \mathbb{P}_1,\ K \in \mathcal{T}_h\}, \tag{23}$$

where $\mathbb{P}_1$ is the space of all polynomials of degree not larger than one. Then, the infinite dimensional space V is approximated by a finite dimensional space $V_h = (Q_h, H_h, R_h)$ and the corresponding discrete approximations $\boldsymbol{u}_h = (p_h, \boldsymbol{v}_h, \boldsymbol{w}_h)$ are determined in the finite element spaces

$$Q_h := S_h/\mathbb{R}, \quad H_h := (S_h)^2, \quad R_h := (S_h)^{n_s+1}. \tag{24}$$

The main observation is now that a simple replacement of V by V_h in (21) does not give a stable discretization. Instead, we use pressure stabilization and streamline diffusion to enhance the main diagonal of the resulting algebraic system. This gives the finite element approximation

$$\boldsymbol{u}_h \in V_h: \quad A(\boldsymbol{u}_h, \boldsymbol{\phi}) + S_h(\boldsymbol{u}_h, \boldsymbol{\phi}) = 0 \quad \text{for all } \boldsymbol{\phi} \in V_h \tag{25}$$

with the stabilization term S_h defined by

$$S_h(\boldsymbol{u}_h, \boldsymbol{\phi}) := c_h(\boldsymbol{u}_h, \theta) + m_h(\boldsymbol{u}_h, \chi) + \sum_{i=0}^{n_s} t_{i,h}(\boldsymbol{u}_h, \pi_i), \tag{26}$$

where

$$c_h(\boldsymbol{u}_h,\theta) := \sum_{K\in\mathcal{T}_h} \alpha_K\big((\boldsymbol{\beta}\cdot\nabla)\boldsymbol{v} + \nabla p_{\text{hyd}} - \rho\mathbf{g}, \nabla\theta)\big)_K, \tag{27}$$

$$m_h(\boldsymbol{u}_h,\chi) := \sum_{K\in\mathcal{T}_h} \delta_K\big((\boldsymbol{\beta}\cdot\nabla)\boldsymbol{v} + \nabla p_{\text{hyd}} - \rho\mathbf{g}, \boldsymbol{\beta}\cdot\nabla\chi)\big)_K, \tag{28}$$

$$t_{i,h}(\boldsymbol{u}_h,\pi_i) := \sum_{K\in\mathcal{T}_h} \delta_{K,i}\Big((\overline{\boldsymbol{\beta}}\cdot\nabla)w_{h,i} - f_i(\boldsymbol{w}_h), \overline{\boldsymbol{\beta}}\cdot\nabla\pi_i)\Big)_K,\ i=0,\dots,n_s. \tag{29}$$

Here, $(\cdot,\cdot)_K$ stands for the inner product over the triangle K. The density ρ_h is a function of $\boldsymbol{w}_h$ and determined from the equation of state in (12). The mesh-dependent constants α_k, β_K, and $\beta_{K,i}$ must be chosen carefully in order to locally reflect convection-dominated as well as diffusion-dominated flows in an appropriate manner. We follow Reference 12 and set in each element $K\in\mathcal{T}_h$,

$$\alpha_K = \frac{h_K^\sharp}{2V}\frac{Re}{\sqrt{1+(Re)^2}},\quad Re := \frac{h_K^\sharp V}{\mu}, \tag{30}$$

$$\beta_K = \frac{h_K}{2|\boldsymbol{v}|}\frac{Re}{\sqrt{1+(Re)^2}},\quad Re := \frac{h_K|\boldsymbol{\beta}|}{\mu}, \tag{31}$$

$$\beta_{K,i} = \frac{h_K}{2|\boldsymbol{v}|}\frac{Re}{\sqrt{1+(Re)^2}},\quad Re := \frac{h_K|\overline{\boldsymbol{\beta}}|}{\nu_i},\quad i=0,\dots,n_s, \tag{32}$$

where V denotes a global reference velocity, $h_K^\sharp$ is the diameter of the 2D ball having the same area as K, and h_K is the length of the element K in the direction of the local velocity $\boldsymbol{v}$.

The highly nonlinear system (25) is often hard to solve without the knowledge of a good initial guess. A common technique is the use of a homotopy approach in order to stabilize Newton's method. This can be best realized by a pseudo implicit time-stepping scheme. We formally add time derivatives to equation (25), resulting in

$$\boldsymbol{u}_h(t)\in V_h:\quad (P\partial_t\boldsymbol{u}_h(t),\boldsymbol{\phi}) + A(\boldsymbol{u}_h(t),\boldsymbol{\phi}) + S_h(\boldsymbol{u}_h(t),\boldsymbol{\phi}) = 0 \quad \text{for all } \boldsymbol{\phi}\in V_h, \tag{33}$$

with a projection matrix $P=\text{diag}(0,1,1)$. In this way, the hydrodynamic pressure p_{hyd} is still determined by a stationary equation and therefore the characteristic property of the low-Mach number model is preserved. Since an accurate resolution of $\boldsymbol{u}_h(t)$ is not important, we solve (33) with the linearly implicit Rosenbrock method ROS3PL[13] employing variable step sizes and a low tolerance until a stationary solution is obtained. This method has very good stability properties and is suitable for the solution of differential-algebraic equations like (33).

3 | THE MOVING MESH METHOD

3.1 | Basic formulation of the moving mesh PDE

In what follows, we will adopt the time-dependent moving mesh method described in References 6,14 to stationary combustion problems. The mesh equation is formulated in terms of a coordinate transformation between the original physical domain Ω and a computational domain Ω_C which has the same topology. We denote the corresponding coordinates by $\boldsymbol{x}=(x_1,\dots,x_n)^T$ and $\boldsymbol{\xi}=(\xi_1,\dots,\xi_n)^T$. The time-depending mapping $\boldsymbol{x}(\boldsymbol{\xi},t):\ \Omega_C\to\Omega$ is defined by the minimizer of the quadratic functional

$$I[\boldsymbol{\xi}] = \frac{1}{2}\int_\Omega\left(\sum_i \nabla\xi_i^T\boldsymbol{G}^{-1}\nabla\xi_i\right)d\boldsymbol{x}, \tag{34}$$

where $\boldsymbol{G}$ stands for the so-called monitor function that links to the physical solution and is used to control the mesh density. Using a variational approach, the minimizer is approximated by the smooth solution of a modified gradient flow equation which reads

$$\frac{\partial \boldsymbol{\xi}}{\partial t} = -\frac{B}{\tau}\frac{\delta I}{\delta \boldsymbol{\xi}} = \frac{B}{\tau}\nabla \cdot (\boldsymbol{G}^{-1}\nabla \boldsymbol{\xi}). \tag{35}$$

Here, $\tau > 0$ is a user specified parameter that controls the response time of the mesh movement and B is a balance function to control the spatial movement of the mesh points. In order to compute the mapping $\boldsymbol{x}(\boldsymbol{\xi}, t)$ directly, we interchange the roles of dependent and independent variables. The final form of the MMPDE can be expressed in the following form:

$$\tau \frac{\partial \boldsymbol{x}}{\partial t} = B\left(\sum_{i,j} A_{ij}\frac{\partial^2 \boldsymbol{x}}{\partial \xi_i \partial \xi_j} - \sum_i b_i \frac{\partial \boldsymbol{x}}{\partial \xi_i}\right), \tag{36}$$

where

$$A_{ij} := \nabla \xi_i^T \boldsymbol{G}^{-1}\nabla \xi_j, \quad b_i := \sum_j \nabla \xi_i^T \frac{\partial \boldsymbol{G}^{-1}}{\partial \xi_j}\nabla \xi_j. \tag{37}$$

The parameter B should be determined such that all mesh points move with a uniform time scale. This allows an easier numerical integration of the MMPDE. The most convenient approach[15] to obtain a well spatially balanced MMPDE is to scale the terms on the right-hand side of (36) as follows:

$$B = \frac{1}{\sqrt{\sum_i (A_{ii}^2 + b_i^2)}}. \tag{38}$$

The main advantage of this approach is that the coefficients in the right-hand side of (36) become $\mathcal{O}(1)$. Then, the corresponding equations are $\boldsymbol{x}$- and $\boldsymbol{G}$-scaling invariant, that is, the MMPDE will not change if we rescale the physical domain and the monitor function. This allows to use the positive parameter τ in (36) to adjust the time scale of the mesh movement. In general, a smaller τ results in a faster mesh adaptation with respect to changes in the monitor function $\boldsymbol{G}$, while a larger τ produces slower movement in time.[16,17] Since we only focus on the design of a static quasi-optimal mesh to improve the approximation quality of the stationary solution, it is sufficient to set $\tau = 1$ and to apply a pseudo time-stepping method. For a complete specification of the coordinate transformation, we also need to supply the MMPDE with appropriate boundary conditions. In our applications, we always fix the mesh points on the boundary. For more advanced strategies, we refer to Reference 15.

3.2 | Construction of the monitor function

A general approach for constructing monitor functions $\boldsymbol{G}$ in two dimensions is based on its eigendecomposition,

$$\boldsymbol{G} = \lambda_1 v_1 v_1^T + \lambda_2 v_2 v_2^T, \tag{39}$$

where $\boldsymbol{v}_1$ and $\boldsymbol{v}_2$ are mutually orthogonal normalized eigenvectors of $\boldsymbol{G}$. The eigenvectors of $\boldsymbol{G}$ determine the directions of the mesh adaptation, while the associated eigenvalues dictate the intensity of the concentration of the mesh in these directions.

Given a vector-values quantity of interest $\boldsymbol{\psi}(\boldsymbol{u}_h(\boldsymbol{x}))$ computed from the stationary numerical solution $\boldsymbol{u}_h(\boldsymbol{x})$, a class of monitor functions can be constructed by harmonic mappings.[18] This reads

$$\begin{aligned} v_1 &= \frac{\boldsymbol{\psi}}{\|\boldsymbol{\psi}\|}, \quad v_2 = v_1^{\perp}, \\ \lambda_1 &= \sqrt{1 + \alpha\|\boldsymbol{\psi}\|^2}, \quad \lambda_2 = \tfrac{1}{\lambda_1}, \end{aligned} \tag{40}$$

where α denotes a user-defined intensity parameter. Typical examples for the function $\boldsymbol{\psi}$ are error indicators, curvature, or gradient data taken from certain solution components. Heuristically, the numerical error is larger in regions

where the solution changes dramatically. For example, suppose a numerical scalar solution u_h exhibits a steep front and the solution gradient is chosen to be one of the eigenvectors, that is, $\boldsymbol{\psi} = \nabla u_h$, then, by using (40), the intensity of the adaptation determined by λ_1 along the normalized gradient direction $\boldsymbol{v}_1$ is much stronger than those determined by λ_2 in the tangential direction $\boldsymbol{v}_2$. Thus, it is expected that coordinate expansion and compression will mainly occur in the gradient direction. However, it should be pointed out that using the solution gradient as $\boldsymbol{\psi}$ may not always be the best option for some problems. This topic will be discussed in our applications. Similar conclusion can already be found in Reference 16.

The monitor function $\boldsymbol{G}$ is usually constructed by nonsmooth operations applied to the numerical solutions. This can result in very stiff MMPDEs. A usual remedy is to smooth the monitor function. Let $\boldsymbol{x}_p$ be a mesh point in Ω and $\boldsymbol{\xi}_p$ the corresponding mesh point in Ω_c. Then the following smoothing algorithm has proven to work quite satisfactorily in practice:[15,19]

$$\begin{aligned} \boldsymbol{G}^0(\boldsymbol{x}_p) &:= \boldsymbol{G}(\boldsymbol{x}_p) && \text{for all grid points } \boldsymbol{x}_p, \\ \boldsymbol{G}^{m+1}(\boldsymbol{x}_p) &:= \frac{\int_{C(\xi_p)} \boldsymbol{G}^m(\boldsymbol{x}_p(\xi))\, d\xi}{|C(\xi_p)|} && \text{for all grid points } \boldsymbol{x}_p, \\ & && m = 0, 1, \ldots, M_s - 1, \end{aligned} \tag{41}$$

with $C(\boldsymbol{\xi}_p) \subset \Omega_C$ is the union of neighboring grid cells having $\boldsymbol{\xi}_p$ as their common vertex. Here, the initial monitor function $\boldsymbol{G}(\boldsymbol{x}_p)$ is directly obtained from (39) and (40). M_s is a user-specified parameter standing for the number of the smoothing cycles to be performed. A smaller M_s gives a more accurate description of the profiles of the monitor function, since it characterizes the exact features of the solutions. However, this usually makes the MMPDE harder to solve. Generally, the value of the intensity parameter α and M_s are problem-dependent.

4 | APPLICATIONS

In this section, we present two reactive flow problems which have an increasing degree of complexity. Both problems have been extensively studied in References 9,11. The first example is the ozone decomposition flame. The chemical processes are modelled with three species and six elementary chemical reactions. The motivation for this application is to demonstrate and compare the numerical results for various monitor functions. Benefits and shortcomings of the moving mesh method will also be discussed. The second example describes a methane flame in a complex geometry. The underlying chemical model contains 15 species and 84 elementary reactions. Some intermediate species have extremely thin flame layers that need to be resolved sufficiently. Furthermore, the whole process possesses both extremely fast and slow motions, implying a strict requirement on the time resolution. All transport coefficients for viscosity, thermal conductivity, and diffusion are evaluated from kinetic models collected in the databases of the Sandia National Laboratories.[20] The influence of the gravitation is neglected, that is, we set $\boldsymbol{g} = 0$ in our applications.

4.1 | A 2D example for ozone decomposition

We use the mechanism for ozone decomposition reaction that consists of 6 elementary reactions proposed in Reference 21:

$$\mathrm{O_3 + M} \underset{2}{\overset{1}{\rightleftharpoons}} \mathrm{O_2 + O + M}, \tag{42}$$

$$\mathrm{O + O + M} \underset{4}{\overset{3}{\rightleftharpoons}} \mathrm{O_2 + M}, \tag{43}$$

$$\mathrm{O + O_3} \underset{6}{\overset{5}{\rightleftharpoons}} \mathrm{O_2 + O_2}. \tag{44}$$

Here, M denotes an arbitrary third body, that is, it can be one of three considered species: oxygen atoms O, oxygen molecules O_2 or ozone O_3. Further details of the reaction mechanism based on the Arrhenius law can be found in Reference [9, table A.1].

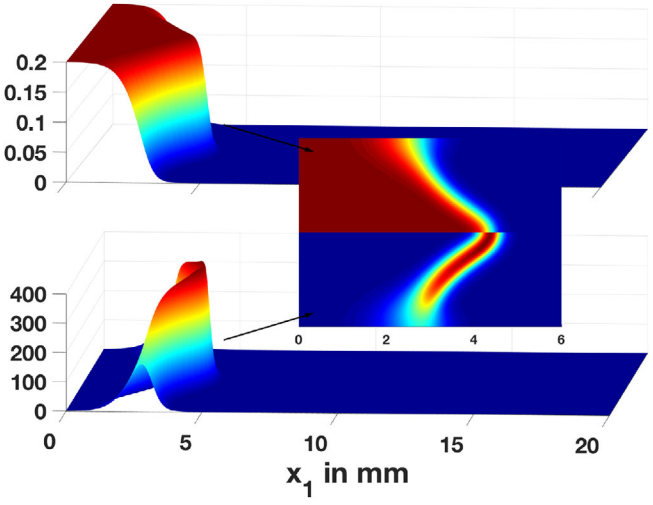

FIGURE 1 Profiles of the numerical solution $w_{O_3,h}$ (top) and its recovered gradient $|D^1 w_{O_3,h}|$ (bottom) [Colour figure can be viewed at wileyonlinelibrary.com]

4.1.1 | Specification of the simulation

The geometry of the simulation is supposed to consist of two flat plates (regarded as rigid walls) with an inflow at the left side, comprising a cold mixture of ozone and oxygen molecules, and a free-stream outflow at the right side. The computational domain is defined as $\Omega :=]0, 0.02[\times]0, 0.005[$ and $\partial\Omega = \Gamma_{\text{in}} \cup \Gamma_{\text{wall}} \cup \Gamma_{\text{out}}$. The boundary conditions are

$$\text{inflow on } \Gamma_{\text{in}}: \quad \boldsymbol{v} = \boldsymbol{v}_{in},\ T = T_{in},\ \boldsymbol{w} = \boldsymbol{w}_{in}, \tag{45}$$

$$\text{rigid walls on } \Gamma_{\text{wall}}: \quad \boldsymbol{v} = 0,\ T = T_{wall},\ \nabla \boldsymbol{w} \cdot \boldsymbol{n} = 0, \tag{46}$$

$$\text{outflow on } \Gamma_{\text{out}}: \quad -\mu \nabla \boldsymbol{v} \cdot \boldsymbol{n} + p\boldsymbol{n} = 0,\ \nabla T \cdot \boldsymbol{n} = 0, \nabla \boldsymbol{w} \cdot \boldsymbol{n} = 0. \tag{47}$$

The initial mass fractions of species are $\omega_{O_3} = 0.2$, $\omega_{O_2} = 0.8$ and the initial temperature is

$$T(x) = 298 + (800 - 298)\ e^{-10^5 (x_1 - 0.005)^2}, \tag{48}$$

which is kept fixed at the inflow and at the rigid wall as Dirichlet boundary conditions. The velocity profile on the inflow boundary is parabolic with a maximum velocity of 0.25 m/s. The Reynolds number is approximately $Re = v_c L/\mu \approx 62$, where v_c is the mean value of the velocity at the inlet, L stands for the length of the geometry, and μ is the viscosity of the mixture at the inflow.

A good indicator of the correct location of the flame front is the mean value of ω_{O_3},[9]

$$J(\boldsymbol{u}) = \frac{1}{|\Omega|} \int_{\Omega} w_{O_3}\ d\boldsymbol{x}. \tag{49}$$

The profiles of the numerical approximation of w_{O_3} and its gradient are shown in Figure 1. We will use $J(\boldsymbol{u}_h)$ to demonstrate the performance of our moving mesh approach. To compare the accuracies for different meshes, we first compute a reference solution with an adaptive, locally refined mesh with about 45 000 grid points using the KARDOS software[22,23] and provide also values for regular meshes with different numbers of uniform grid points. The results are collected in Table 1.

4.1.2 | A first monitor function

A central issue when applying a moving mesh method is to define a proper monitor function to control the distribution of the grid points. In most cases, the monitor function should ensure that the grid points are concentrated in regions where

TABLE 1 Values for $J(\boldsymbol{u}_h)$ defined in (49) for uniform meshes with different numbers of points (noP) and absolute values of the numerical errors $J(\boldsymbol{e}) = J(\boldsymbol{u} - \boldsymbol{u}_h)$ derived from an adaptive reference solution with about 45 000 grid points

noP	$J(\boldsymbol{u}_h)$	$\lvert J(\boldsymbol{e})\rvert$
1105	0.03331313	1.912892×10^{-4}
2835	0.03347317	1.570370×10^{-4}
4257	0.03348598	1.844070×10^{-5}
Adaptive	0.03350442	–

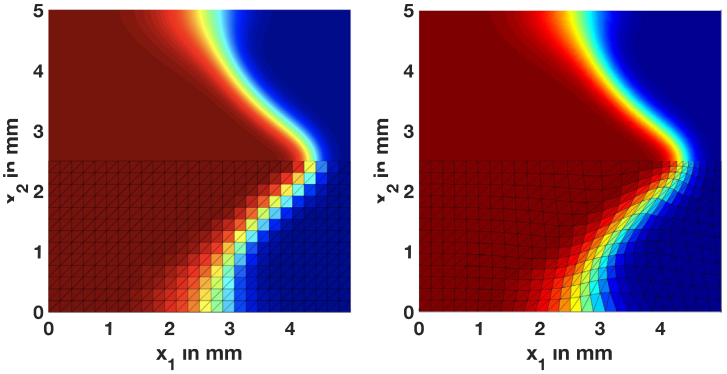

FIGURE 2 Comparison of the numerical solution $w_{O_3,h}$ computed on uniform and adaptive meshes. Left: numerical solution $w_{O_3,h}$ with high resolution computed on a uniform mesh with 148 417 grid points (above) and with low resolution on a uniform mesh with 2835 grid points (below). Right: numerical solution $w_{O_3,h}$ with high resolution computed on a regular mesh with 148 417 grid points (above) and on an adaptive mesh with 2835 grid points (below) [Colour figure can be viewed at wileyonlinelibrary.com]

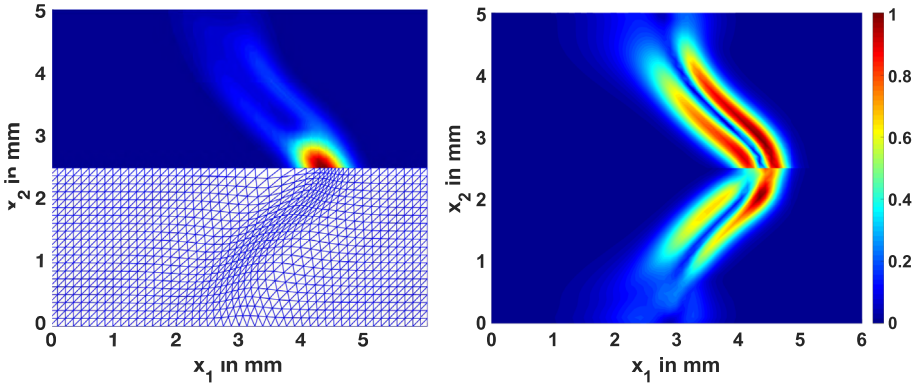

FIGURE 3 Left: 2D plot of the mesh density $\sqrt{\det(\boldsymbol{G}(D^1 w_{O_3,h}(\boldsymbol{x})))}$ after smoothing (above) and corresponding adaptive moving mesh (below). Right: error distribution of the mass fraction of ozone molecules ω_{O_3}; approximate interpolation error indicator (above) and hierarchical basis error estimator (below) [Colour figure can be viewed at wileyonlinelibrary.com]

the physical solutions require a higher resolution. So the grid points on a uniform mesh should be relocated so that the requirement on the number of the mesh cells necessary to appropriately resolve a flame layer can be satisfied.[24] Common practice when constructing a monitor function is to employ some heuristic choices. For problems where the solutions change dramatically within a small region, such as the flame layer of the ozone molecules ω_{O_3} illustrated in Figure 1, there are usually larger numerical errors in regions with large gradients. Thus, the gradients of certain solution components often represent a good error indicator. The gradient of a piecewise linear function is a constant vector in each element $K \in \mathcal{T}_h$. In order to improve the approximation property, we apply a standard gradient recovery operator $D^1 : S_h \to (S_h)^2$ as introduced in Reference 25, and choose in our first experiment

$$\boldsymbol{\psi} := D^1 w_{O_3,h}, \tag{50}$$

as eigenvector $\boldsymbol{v}_1$ of the monitor function $\boldsymbol{G}$ to enforce a mesh adaption in this direction. From Figure 2, we can make the following observations: The contour of the flame layer becomes more distinct and can be better approximated through adjusting the locations of the grid points close to the sharp flame front. The mesh cells are compressed to different extents along the convective direction of the flow so that an obvious anisotropic behavior is visible. Moreover, the mesh points are correctly concentrated in the area where the gradient is large. This is exactly the location where the mesh density takes its peak values, as illustrated in Figure 3. However, Table 2 shows that the accuracy of $J(\boldsymbol{u}_h)$ does not always improve with increasing grid points as one would expect. A similar behavior has been observed in Reference 15.

noP	$J(\boldsymbol{u}_h)$, uniform	$J(\boldsymbol{u}_h)$, adaptive	$\lvert J(\boldsymbol{e})\rvert$, uniform	$\lvert J(\boldsymbol{e})\rvert$, adaptive
1105	0.03331313	0.03356365	2.912892×10^{-4}	5.918997×10^{-5}
2835	0.03347317	0.03344742	1.570370×10^{-4}	5.703389×10^{-5}
4257	0.03348598	0.03344386	1.844070×10^{-5}	6.059835×10^{-5}

The reference value is $J(\boldsymbol{u}) \approx 0.03350442$.

TABLE 2 Results for uniform and moving meshes with the quantity of interest $\boldsymbol{\psi} = D^1 w_{O_3,h}$ and parameters $M_s = 8$ and $\alpha = 80$ for the moving mesh design

In the following, we would like to discuss two reasons for this behavior. First, while the grid points are concentrated in regions with large gradients of $w_{O_3,h}$, the accuracy of the other components, which also influence the balance of O_3, might be lower due to certain local expansions of mesh lines, resulting in a worse accuracy for $J(\boldsymbol{u}_h)$. Second, although regions of large solution gradients can usually reflect areas with large numerical errors, this is not always true for the exact error distribution. Because of the coupling of all components, using the gradient of a single component may lead to an over-concentration of mesh points in areas that have already been sufficiently resolved. The right graph in Figure 3 illustrates an estimated error distribution which is based on a hierarchical error estimator proposed in Reference 23. Obviously, the error distribution differs significantly from the density function illustrated in the left graph in Figure 3, which governs the concentration of the grid points in the MMPDE. The error distribution has a double-layer structure, where the numerical errors are mainly accumulated in regions with large flame curvature. More specifically, at the downstream edge, the numerical errors are larger than those on the upstream side. The downstream edge of the flame layer is located in a transitional reaction zone, where the dynamics of the species is governed by both convection and source terms. There the intermediate species are also frequently produced and consumed. Thus, a higher resolution in this region is preferable. Next we will construct a monitor function which is based on local error information.

4.1.3 | A second monitor function

Now, we will introduce a second monitor function which is based on an approximate interpolation error indicator. First, we recall the Sobolev space $H^2(\Omega)$ which consists of all functions from $H^1(\Omega)$ with square-integrable generalized second-order derivatives. In what follows, we will denote by $|\cdot|_{H^i}, i = 1, 2$, the usual semi-norm in H^i defined by derivatives of i-th order only. Let $u \in H^2(\Omega) \cap C^0(\overline{\Omega})$, for the moment, be a scalar solution, u_h its linear finite element approximation, and $\Pi_1 u \in S_h$ its linear interpolant defined by $u(\boldsymbol{x}_i) = \Pi_1 u(\boldsymbol{x}_i)$ for all mesh points $\boldsymbol{x}_i$. Then a standard argument for the interpolation error

$$|u - \Pi_1 u|_{H^1(\Omega)} = \left(\sum_{K \in \mathcal{T}_h} |u - \Pi_1 u|_{H^1(K)} \right)^{1/2} \leq C \sum_{K \in \mathcal{T}_h} h_K |u|_{H^2(K)}, \tag{51}$$

gives the a priori error estimate for the linear finite element solution,

$$\|u - u_h\|_{H^1(\Omega)} \leq Ch|u|_{H^2(\Omega)}, \tag{52}$$

where $h := \max_{K \in \mathcal{T}_h} h_K$. This, together with the observations made in the previous section, motivates to use second derivatives of u_h to control the local density of the moving mesh. An approximation $D^2 u_h \in (S_h)^2$ for $(\partial_{x_1 x_1} u, \partial_{x_2 x_2} u)^T$ is derived from a quadratic interpolation of u_h [16, section 4.2]. Then, we set for our application,

$$\boldsymbol{\psi} := D^2 w_{O_3,h}. \tag{53}$$

We would like to mention that this choice is in line with the Hessian-based monitor function proposed by Huang and Li,[26] where the second derivatives are used to control the error with respect to functionals in an optimal manner. It reads in our case

$$|J(u) - J(u_h)| = \frac{1}{|\Omega|} \left| \int_\Omega (w_{O_3} - w_{O_3,h})\, dx \right| \rightarrow \text{Minimize!} \tag{54}$$

In Figure 4, the profile of $w_{O_3,h}$ and its approximate interpolation error indicator $|D^2 w_{O_3,h}|$ are shown. We observe that this error indicators gives nearly as good information on the local errors as the more sophisticated error estimator based

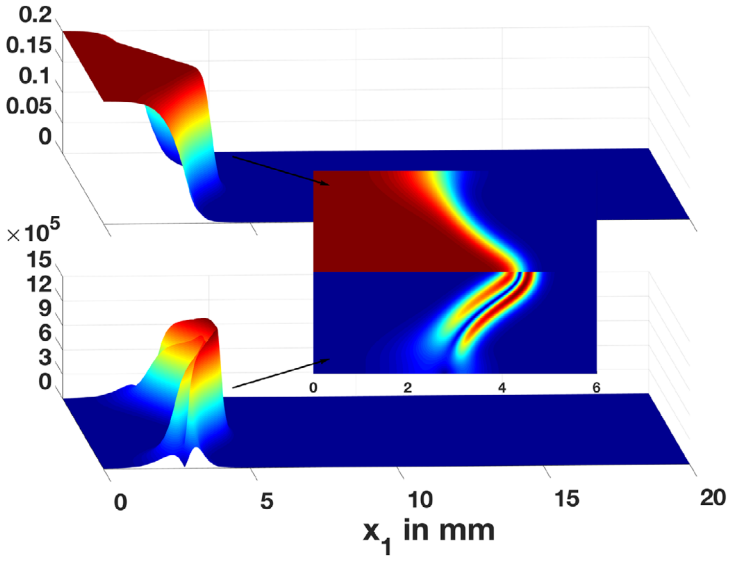

FIGURE 4 Profiles of the numerical solution $w_{O_3,h}$ (top) and its interpolation error indicator $|D^2 w_{O_3,h}|$ (bottom) [Colour figure can be viewed at wileyonlinelibrary.com]

TABLE 3 Computation results for moving meshes with two monitor function based on the gradient $D^1 w_{O_3,h}$ (gradient) and on the interpolation error indicator $D^2 w_{O_3,h}$ (interr) with $M_s = 8$, $\alpha = 80$

noP	$J(u_h)$, gradient	$J(u_h)$, interr	$\lvert J(e)\rvert$, gradient	$\lvert J(e)\rvert$, interr
2835	0.03344742	0.03344717	5.703389×10^{-5}	3.272824×10^{-5}
4257	0.03344386	0.03504592	6.059835×10^{-5}	1.347509×10^{-7}

The reference value is $J(\boldsymbol{u}) \approx 0.03350442$.

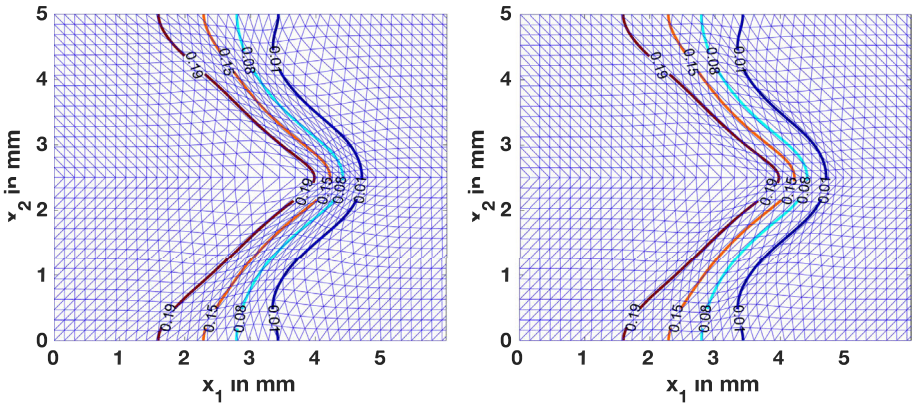

FIGURE 5 Comparisons of moving meshes generated by different monitor functions for 4257 mesh points. Color curves represent the contour lines of ω_{O_3}. Left: Close-up view of the adaptive mesh around the O_3-flame layer computed by the gradient-based function $\psi = D^1 w_{O_3,h}$. Right: Close-up view of the adaptive mesh around the O_3-flame layer computed by the second derivative-based function $\psi = D^2 w_{O_3,h}$ [Colour figure can be viewed at wileyonlinelibrary.com]

on a hierarchical basis, compare Figure 3, but is much cheaper. From Table 3, we see that the results obtained by using the new monitor function are much better than those based on the gradient of $w_{O_3,h}$. From a comparison of both methods shown in Figure 5, it becomes visible that with the new monitor function grid points are concentrated in a larger area due to the higher second derivatives and hence numerical errors.

4.2 | A 2D example for methane combustion

In this section, we consider a methane combustion problem described by the following global reaction

$$CH_4 + 2O_2 \rightarrow CO_2 + 2H_2O. \tag{55}$$

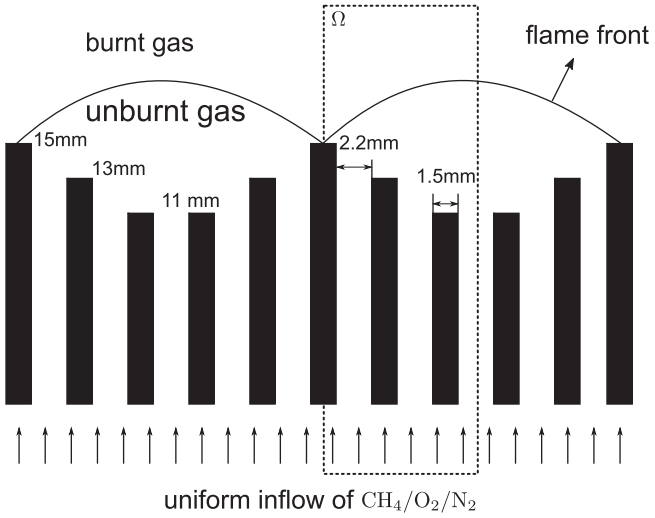

FIGURE 6 Geometry of the methane burner considered

The reaction mechanism with 15 species and 84 elementary reactions is taken from Reference 27. We will consider a lamella burner which is modified from a prototype constructed by JUNKERS Bosch Thermotechnik.[28] The geometry for the simulation is given in Figure 6.

4.2.1 | Specification of the simulation

A stoichiometric mixture of methane (CH_4) and air (O_2/N_2) flows from the bottom of the burner through a sample of slots which have a uniform width interval of 2 mm and three different heights varying from 15 mm to 11 mm. All slots have the same width of 1.5 mm. The inflow velocity is $v_2 = 0.27$ m/s. The solution is assumed to be spatially periodic. Thus it is sufficient to restrict the computational domain to three slots which define Ω, see Figure 6. The lamellae can be considered as obstacles. Dirichlet boundary conditions are used for the temperature, no-slip conditions for the velocities, and Neumann boundary conditions for the species on the wall of the lamellae. To specify the temperature on the wall of the slots, we use three piecewise linear functions varying from 298 K to 393 K, 453 K, and 463 K, respectively. On the cut boundary of Ω, symmetric boundary conditions are used for all the variables. For more details, we refer to References 9,11,29.

This problem is characterized by the interaction of different physical processes and largely separated scales. A simulation on uniform meshes can be very prohibitive. We expect that moving mesh strategies designed with an appropriate monitor function will improve the numerical approximation even on relatively coarse meshes.

4.2.2 | Application of moving meshes

Since the underlying combustion mechanism is relatively complicated, it is not possible to calculate a stable stationary solution on quasi-uniform meshes with around 40 000 grid points. Higher resolution is needed near the flame front in the reaction zone and in the pre-heating zone, where the chemical and convection-diffusion processes are strongly coupled. These regions are unknown a priori. Therefore, we directly couple the physical PDE with the MMPDE by an arbitrary Lagrangian-Eulerian approach.

We first define $\hat{\boldsymbol{u}}_h(t) := \hat{\boldsymbol{u}}_h(\boldsymbol{x}(\boldsymbol{\xi}, t), t) = \hat{\boldsymbol{u}}_h(\boldsymbol{\xi}, t)$. Under the mapping $\boldsymbol{x}(\boldsymbol{\xi}, t)$, we then transform (33) into a system involving the computational coordinates $\boldsymbol{\xi}$, that is,

$$\begin{aligned} \hat{\boldsymbol{u}}_h(t) \in V_h \,:\, & \left(P\left(\partial_t \hat{\boldsymbol{u}}_h(t) - (\partial_t \boldsymbol{x} \cdot J^{-T}\hat{\nabla})\,\hat{\boldsymbol{u}}_h(t)\right), \boldsymbol{\phi}\right) \\ & + \hat{A}(\hat{\boldsymbol{u}}_h(t), \boldsymbol{\phi}) + \hat{S}_h(\hat{\boldsymbol{u}}_h(t), \boldsymbol{\phi}) = 0 \quad \text{for all } \boldsymbol{\phi} \in V_h. \end{aligned} \tag{56}$$

Here, $\hat{\nabla}$ denotes the gradient operator with respect to $\boldsymbol{\xi}$ and $J = \partial \boldsymbol{x}/\partial \boldsymbol{\xi}$ is the Jacobian of the mapping $\boldsymbol{x}(\boldsymbol{\xi}, t)$. The operators $\hat{A}$ and $\hat{S}_h$ are obtained from A and S_h by using the identity $\nabla = J^{-T}\hat{\nabla}$ and replacing $\boldsymbol{u}_h$ by $\hat{\boldsymbol{u}}_h$. The additional term

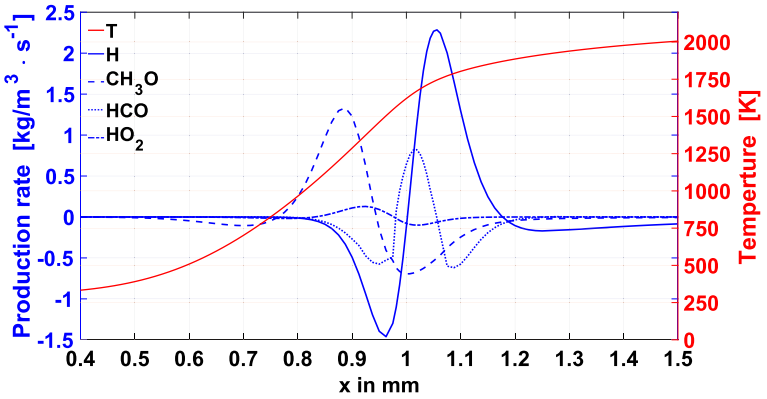

FIGURE 7 1D study of the production rate of some intermediate species. We choose HCO as candidate for the mesh design [Colour figure can be viewed at wileyonlinelibrary.com]

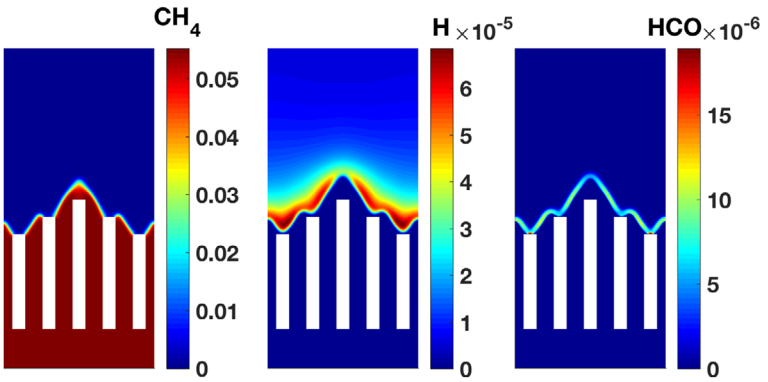

FIGURE 8 Mass fraction of CH_4, H, and HCO at the steady state [Colour figure can be viewed at wileyonlinelibrary.com]

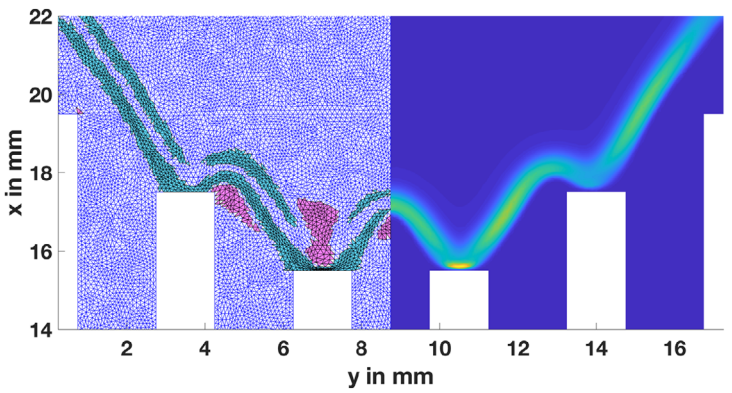

FIGURE 9 Adaptive grid (left) and profile of the radical HCO (right) close to the top of the lamellae at steady state. The elements colored in magenta show enlarged triangles (up to 15%), and the elements colored in cyan illustrate the compressed cells (up to −5%). The mesh resolution is clearly aligned to the flame structure [Colour figure can be viewed at wileyonlinelibrary.com]

$(\partial_t \boldsymbol{x} \cdot J^{-T}\hat{\nabla})\ \hat{\boldsymbol{u}}_h$ on the left side can be viewed as a correction for the convective effects of the mesh motion. Note that the linear finite element space V_h is now related to a time-independent regular partition of triangles of the computational domain Ω_C. Equation (56) is simultaneously solved with the MMPDE defined in (36) in the course of the pseudo time-stepping method. The location of the mesh points described by the mapping $\boldsymbol{x}(\boldsymbol{\xi}, t)$ is immediately adapted to the evolving flame structure until the stationary state is reached. Adjusting the mesh points in this way yields a stable numerical solution, even on relatively coarse meshes. In our calculation, we start with an isotropic quasi-uniform mesh with 29 864 grid points delivered from the 2D-mesh generator TRIANGLE.[30] We first compute the temperature-dependent flow field without combustion and then start our mesh moving approach including all reaction terms.

For the choice of the monitor function, we study a 1D simplification of the chemical reaction process. A corresponding simulation shows that the formyl radical HCO and its production rate have an extremely thin flame layer, see Figure 7. Moreover, both are very sensible with respect to insufficient mesh resolution.[29] Hence, w_{HCO} is a good candidate for the mesh design. We set $\boldsymbol{\psi} = D^2 w_{\mathrm{HCO},h}$, which is now updated in each time step. In Figure 8, we show the mass fraction of CH_4, H, and HCO at the steady state. The thin reaction zone of HCO is clearly visible. A closer look at the top of the lamellae presented in Figure 9 and Figure 10 reveals that the mesh cells are strongly compressed there and aligned with respect to the flame structure. Their areas are correspondingly reduced.

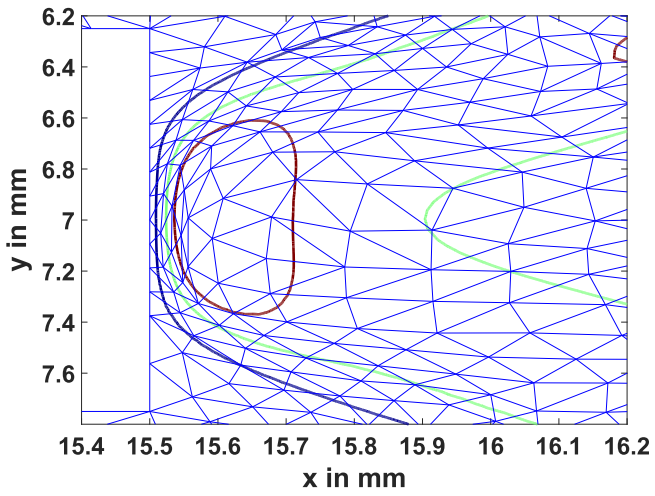

FIGURE 10 Resolution of the flame layer of HCO at the top of the hottest lamella. Color curves represent contour lines of the mass fraction of HCO: blue/green/brown correspond to 0.1, 0.3, $0.5 * \|w_{HCO,h}\|_\infty$, respectively [Colour figure can be viewed at wileyonlinelibrary.com]

We would like to mention that the detection of the formyl radical HCO is also of great interest since it can provide information about the local heat release rate which is a key parameter in the understanding of combustion processes. Due to the low signal level, some optical diagnostic techniques, such as HCO planar laser-induced fluorescence (PLIF), are not capable for visualization and quantitative measurements.[31] Thus, the numerical investigation of the dynamic behavior of this radical can reveal more information for further research.

5 | CONCLUSIONS

In this article, we have presented a 2D adaptive moving mesh method based on combustion-specific design criteria in order to improve the numerical resolution of steady state premixed flames in the low Mach number regime. We have discussed the key ideas needed to design moving meshes which allow a relocation of mesh points without changing their connectivity. An iterative and simultaneous moving mesh strategy that balances solution gradients or interpolation errors over the whole spatial mesh have been applied to two combustion problems in 2D: a ozone decomposition and a methane flame for a lamella burner. In both simulations, a curvature-based adaptation of the mesh points yielded an improved flame resolution and a stable calculation of the steady state. Adaptive moving meshes led to an enhanced simulation capability that has made it possible to simulate realistic flames without using more sophisticated local mesh refinement methods.

ACKNOWLEDGEMENTS

Z. Sun and J. Lang were supported by the Deutsche Forschungsgemeinschaft within the Graduate School of Excellence Energy Science and Engineering at Technical University of Darmstadt (DFG GSC1070).

CONFLICT OF INTEREST

The authors declare no potential conflict of interest.

ORCID

Jens Lang https://orcid.org/0000-0003-4603-6554

REFERENCES

1. Bell J, Day M. Adaptive methods for simulation of turbulent combustion. In: Echekki T, Mastorakos E, eds. *Turbulent Combustion Modeling, Volume 95 of Fluid Mechanics and Its Applications*. Dordrecht, Netherlands: Springer; 2011:301-329.
2. Becker R, Braack M, Rannacher R. Numerical simulation of laminar flames at low mach number with adaptive finite elements. *Combust Theory Model*. 1999;3:503-534.
3. Braack M, Richter T. Stabilized finite elements for 3D reactive flows. *Int J Numer Methods Fluids*. 2006;51:981-999.
4. Fröhlich J, Lang J. Twodimensional cascadic finite element computations of combustion problems. *Comp Meth Appl Mech Eng*. 1998;158:255-267.

5. Lang J. High-resolution self-adaptive computations on chemical reaction-diffusion problems with internal boundaries. *Chem Eng Sci*. 1996;51:1055-1070.
6. Huang W, Russell R. *Adaptive Moving Mesh Methods*. Applied Mathematical Sciences. New York, NY: Springer; 2010.
7. Liersch C, Frankenbach M, Fröhlich J, Lang J. Recent progress in designing moving meshes for complex turbulent flows. *Meteorol Z*. 2014;23:425-439.
8. Madja A, Sethian J. The derivation and numerical solution of the equation for zero mach number of combustion. *Combust Sci Technol*. 1985;42:185-205.
9. Braack M, Rannacher R. Adaptive finite element methods for low-Mach-number flows with chemical reaction. Proceedings of the 30th Computational Fluid Dynamics, Volume 3 of Lecture Series von Karman Institute; 1999:1-93.
10. Smooke MD, Giovangigli V. Formulation of the premixed and nonpremixed test problems. In: Smooke MD, ed. *Reduced Kinetic Mechanisms and Asymptotic Approximations for Methane-Air Flames*. Berlin, Heidelberg: Springer; 1991:1-28.
11. Braack M. *An Adaptive Finite Element for Reactive Flow Problems* (PhD thesis). Universität Heidelberg; 1998.
12. Lang J. Adaptive incompressible flow computations with linearly implicit time discretization and stabilized finite elements. In: Papailiou KD, Tsahalis D, Periaux J, Hirsch C, Pandolfi M, eds. *Computational Fluid Dynamics '98*. New York, NY: John Wiley & Sons; 1998:200-204.
13. Lang J, Teleaga D. Towards a fully space-time adaptive FEM for magnetoquasistatics. *IEEE Trans Magn*. 2008;44:1238-1241.
14. Huang W, Ren Y, Russell R. Moving mesh methods based on moving mesh partial differential equations. *J Comput Phys*. 1994;113:279-290.
15. Huang W. Practical aspects of formulation and solution of moving mesh partial differential equations. *J Comput Phys*. 2001;171:753-775.
16. Cao W, Huang W, Russell R. Comparison of two-dimensional r-adaptive finite element methods using various error indicators. *Math Comput Simul*. 2001;56:27-143.
17. Cao W, Huang W, Russell R. An error indicator monitor function for an r-adaptive finite-element method. *J Comput Phys*. 2001;170:871-892.
18. Cao W, Huang W, Russell R. A study of monitor functions for two dimensional adaptive mesh generation. *SIAM J Sci Comput*. 1999;20:1978-1994.
19. Lang J, Cao W, Huang W, Russel R. A two-dimensional moving finite element method with local refinement based on a posteriori error estimates. *Appl Numer Math*. 2003;46:75-94.
20. Kee R, Rupley F, Miller J. The Chemkin Thermodynamik Data Base. Technical Report SAND87-8215.UC4, Sandia National Laboratories; 1987.
21. Warnatz J. Calculation of the structure of laminar flat flames i: flame velocity of freely propagating ozone decomposition flames. *Bericht der Bunsen-Gesellschaft für physikalische Chemie*. 1978;82:193-200.
22. Erdmann B, Lang J, Roitzsch R. *KARDOS User's Guide*. Berlin, Germany: Konrad-Zuse-Zentrum; 2002.
23. J. Lang. *Adaptive Multilevel Solution of Nonlinear Parabolic PDE Systems. Theory, Algorithm, and Applications, Volume 16 of Lecture Notes in Computational Science and Engineering*. Berlin, Germany: Springer-Verlag; 2000.
24. Poinsot T, Veynante D. *Theoretical and Numerical Combustion*. 3rd ed. Philadelphia, PA: Edwards; 2012.
25. Zienkiewicz OC, Zhu J. The superconvergent patch recovery and a posteriori error estimates. part 1: the recovery technique. *Int J Numer Methods Eng*. 1992;33:1331-1364.
26. Huang W, Li X. An anisotropic mesh adaptation method for the finite element solution of variational problems. *Finite Elem Anal Des*. 2010;46:61-73.
27. Smooke MD. Numerical modeling of laminar diffusion flames. In: Oran ES, Boris JP, eds. *Progress in Astronautics and Aeronautics*. Vol 135. Reston VA: AIAA; 1991.
28. Parmentier S, Braack M, Riedel U, Warnatz J. Modeling of combustion in a Lamella burner. *Combust Sci Technol*. 2003;175:173-199.
29. Sun Z. Adaptive Moving Finite Element Method for Steady Low-Mach-Number Compressible Combustion Problems (PhD thesis). Technische Universität Darmstadt; 2018.
30. Shewchuk J. Delaunay refinement algorithms for triangular mesh generation. *Comput Geomet Theory Appl*. 2002;23:21-74.
31. Kiefer J, Li ZS, Seeger T, Leipertz A, Aldén M. Planar laser-induced fluorescence of HCO for instantaneous flame front imaging in hydrocarbon flames. *Proc Combust Inst*. 2009;32:921-928.

How to cite this article: Sun Z, Braack M, Lang J. An adaptive moving finite element method for steady low Mach number compressible combustion problems. *Int J Numer Meth Fluids*. 2020;92:1081–1095. https://doi.org/10.1002/fld.4818